CO tolerance of Pt and PtSn intermetallic electrocatalysts on synthetically modified reduced graphene oxide supports†

Christopher M. Sims, Audaldo A. Ponce,‡ Karen J. Gaskell and Bryan W. Eichhorn*

Pt and PtSn intermetallic nanoparticle (NP) catalysts were grown directly on various reduced graphene oxide (rGO) supports and were characterized by a combination of X-ray photoelectron spectroscopic (XPS), Raman microscopy, transmission electron microscopy (TEM), and powder X-ray diffraction (XRD) studies. Electrochemical CO stripping and rotating disk electrochemical (RDE) experiments showed the four rGO-PtSn catalysts to be superior to the four rGO-Pt catalysts for CO and CO−H_2 electrooxidation in acidic solutions regardless of the rGO support, in agreement with earlier reports on PtSn NP electrocatalysts. For the four rGO-Pt catalysts, the rGO support causes a 70 mV spread in CO oxidation peak potential (ΔE_{peak}) and a 200 mV spread in CO−H_2 electrooxidation onset. The more oxygenated graphenes show the lowest CO oxidation potentials and the best CO tolerance. For the four rGO-PtSn intermetallic catalysts, a ~160 mV spread in CO−H_2 electrooxidation onset is observed. With the exception of the nitrogen-doped graphene (NGO), a similar trend in enhanced CO electrooxidation properties with increasing oxygen content in the rGO support is observed. The NGO-PtSn electrocatalyst was superior to the other rGO-PtSn catalysts and showed the largest improvement in CO tolerance relative to the pure Pt system. The origin of this enhancement appears to stem from the unique rGO-PtSn support interaction in this system. These results are discussed in the context of recent theoretical and experimental studies in the literature.

Introduction

As a carbon-based support material for nanoparticle (NP) electrocatalysts, graphene is thought to be advantageous over traditional carbon black (CB), due to its large surface area,[1] high electronic conductivity,[2] and relative ease of production.[3,4] While industrial-scale production of pristine graphene sheets is currently impractical, reduced graphene oxides (rGO) are available in large quantities and have been subjected to many studies. In contrast to pristine graphene, rGOs can contain several kinds of functional groups, heteroatoms and defects. Many pathways have been developed for synthesizing rGOs, including one-step thermal exfoliation/reduction,[5,6] high temperature reduction in hydrogen atmosphere,[7] wet chemical reductions,[8–10] and various combinations of these

techniques.[11–13] Different synthetic methods create different functional groups that alter the physical and electronic properties relative to pristine graphene.[5,6,8,14–20] The defects and functional groups in the rGOs alter the interactions between the NP and support and potentially affect the catalytic activity of a system. For example, recent thermal studies have shown that rGO-supported iron-based NP catalysts had markedly better performance in *syn*-gas conversions relative to the same iron-based NP catalysts on carbon nanotubes.[21]

While many electrochemical studies have been conducted on rGO-supported metal NP catalysts,[22–37] the influence of rGO on the electrocatalytic activity of NPs is not well understood. In the context of electrooxidation of hydrogen in the presence of CO impurities (*i.e.* CO tolerance), previous studies[28,36,38] have suggested that rGO-Pt NPs feature improved activity relative to CB-Pt catalysts due to Pt electronic structure modification as a result of strong Pt–graphene interactions. The magnitude of this metal-support interaction is thought to be dependent on the amount and types of chemical defects within the graphene structure.[38–40] Since the chemistry of functionalizing graphene has advanced significantly in recent years, the ability to tune these metal-support interactions through chemical modification of graphene is potentially powerful. Metal-support interactions between NPs and

Department of Chemistry and Biochemistry, University of Maryland, College Park, MD 20742, USA. E-mail: eichhorn@umd.edu

inorganic supports are well known to have significant influences on catalytic activities, but are not tunable in the same way that a graphene system can be modified.[41–43] This research aims to evaluate the influence of different types of modified graphene on electrocatalytic activity with the ultimate goal of developing predictability and control in the design of new electrocatalyst systems.

To evaluate the metal-support interactions between modified graphene and metallic NP catalysts, we describe the full characterization of four different rGOs and their use in preparing rGO-supported Pt and PtSn electrocatalysts catalysts. These electrocatalysts were evaluated for their CO electrooxidation and CO–H_2 electrooxidation activities. Our studies show that the nature of the rGO support material affects the resulting Pt or PtSn NP size. In the case of nitrogen-doped rGOs, an anomalous metal support interaction was found that caused a marked difference in the behavior of the Pt and PtSn systems for CO–H_2 electrooxidation.

Experimental section

Materials

Vor-X graphene powder (FGS, C : O ratio = 22) was provided by Vorbeck Materials. Single layer graphene (SLG, powder) and single layer graphene oxide (GO, flakes) were purchased from ACS Material. Platinum acetylacetonate ($Pt(acac)_2$, 97%), tin chloride ($SnCl_4$, 99%), sodium triethylborohydride solution ($NaBEt_3H$, 1.0 M in toluene), sodium borohydride ($NaBH_4$, 98%), hydrazine monohydrate (H_2NNH_2, 98%), 1-octadecene (90%), and acetone (99.5%) were purchased from Aldrich. Methanol (MeOH, 99.8%) was purchased from VWR. Tetrahydrofuran (THF, 99%) was purchased from Mallinckrodt. Isopropanol (iPrOH, 99%) was purchased from Pharmco-AAPER. Sulfuric acid (H_2SO_4, 96.4%) was purchased from Fisher. Nafion® (5%) solution was purchased from Fluka. E-TEK Pt (30% HP Pt on Vulcan® XC-72) was purchased from BASF. Ultra-pure water was obtained from deionized water using a Millipore Academic Milli-Q A10 purifier system. All materials were used as received without further purification.

Preparation of borohydride-reduced graphene oxide (BGO)

Typically, GO (100 mg) was dissolved in ultra-pure water (40 mL) through sonication in a glass beaker and then transferred into a 100 mL round-bottomed flask. $NaBH_4$ (1 g, 0.026 mol) was added to the solution, which was then heated to 80 °C for 24 h. After cooling to room temperature, the black precipitate was separated by filtration, washed with copious amounts of water, air-dried overnight and dried under reduced pressure for 24 h.

Preparation of hydrazine-reduced graphene oxide (NGO)

The same procedure as above was utilized, except H_2NNH_2 (1 mL, 0.02 mol) was used instead of $NaBH_4$. All other steps were identical.

Synthesis of rGO-supported PtSn intermetallic NPs

In a typical synthesis, rGO (13.3 mg) was mixed with 1-octadecene (10 mL) in a glass vial and sonicated for 2 h in a sonication bath. The resultant mixture was then added to a schlenk flask and degassed at 80 °C while stirring. Once degassed, N_2 was introduced and the temperature was increased to 200 °C. In a separate vial, $Pt(acac)_2$ (10.0 mg, 0.025 mmol Pt) was dissolved in 1-octadecene (1 mL), degassed, and placed under N_2. $SnCl_4$ (3 μL, 0.025 mmol Sn) was then added to the Pt precursor solution while stirring. $NaBEt_3H$ solution (2 mL, 1.0 M) was injected into the rGO dispersion, immediately followed by the injection of the PtSn precursor solution. All injections were performed using N_2-purged syringes. The reaction mixture was returned to 200 °C for 60 min before the heating source was removed. The flask was allowed to cool down to room temperature before the black slurry was transferred to a 50 mL conical centrifuge tube. MeOH (2 mL) and acetone (20 mL) were added to the tube and the resultant mixture was sonicated for 10 min. The tube was then centrifuged at 6000 rpm for 15 min. The supernatant was discarded and the black solid was mixed with ultra-pure water (2 mL) and acetone (10 mL) and sonicated for 10 min. The resultant mixture was divided amongst several 1.5 mL conical centrifuge tubes and centrifuged at 13 000 rpm for 2 min. The supernatant of each tube was discarded and the black solids were mixed with 1 mL acetone, vortexed, then centrifuged at 13 000 rpm for 2 min. The acetone washing process was repeated five times. The black solid was then dried under vacuum for 60 min. The dried solid was placed in a ceramic boat, which was introduced into a quartz glass tube. The tube was heated in a horizontal solid tube furnace (Thermolyne F21135, Thermo Scientific) at 400 °C for 120 min under a 5% H_2/95% Ar atmosphere with a flow rate of 90 cc min^{-1}.

Synthesis of rGO-supported Pt NPs

The same procedure as above was utilized, except $SnCl_4$ was absent and the amount of $Pt(acac)_2$ was increased to maintain the same weight percent loading of metal on rGO (11.5 mg, 0.029 mmol Pt). All other steps were identical.

Sample characterization

Raman spectroscopy data were collected on a Horiba Yvon LabRam ARAMIS Raman microscope using a ~1 mW, 532 nm wavelength laser source. The rGO samples were pressed on a glass slide for analysis. X-ray photoelectron spectroscopy (XPS) data were collected on a Kratos Axis 165 X-ray photoelectron spectrometer operating in the hybrid mode using Al monochromatic radiation (1486.6 eV) at 280 W. Charge neutralization was used to minimize sample charging. Binding energies were calibrated with respect to the C 1s peak at 284.8 eV. Casa XPS software was used for data analysis peak fitting; all peaks were fit after subtraction of a Shirley background. An *ad hoc* asymmetric peak shape (A(0.41, 0.36, 70)GL(50)) was used to fit the primary graphitic carbon peak for all the rGO samples. The π→π* shake-up satellites were fitted to have a full width at half

maximum (FWHM) value of 3.5 at maximum. All other peaks were fixed to have the same FWHM for each sample. Peak positions for C–N, C–O, C=O, COOH, and the $\pi \rightarrow \pi^*$ shake-up satellites were fixed relative to the graphitic peak with separations of 0.9, 1.7, 3.0, 4.3, 6.4 eV respectively. Powder X-ray diffraction (XRD) patterns were obtained on a Bruker C2 Discover diffractometer equipped with a VÅNTEC-500 detector using a monochromatic Cu Kα radiation source biased at 40 kV and 40 mA. The rGO-supported NP powders were pressed on a glass slide for analysis. Transmission electron microscope (TEM) images were obtained on a JEM 2100F Field Emission TEM operating at 200 kV. Energy-dispersive X-ray spectroscopy (EDS) data were collected on the same TEM operating in STEM mode. The rGO-supported NP powders were dispersed in THF, and a 6 µL aliquot of the resulting dispersion was drop cast on the TEM grids. The TEM grids used were lacey carbon-coated Cu grids (Cu-400LC, Pacific Grid Tech).

Electrochemical analysis

iPrOH (159.2 mL), ultra-pure water (40.0 mL) and Nafion® solution (0.80 mL, 5%) were mixed and stored as a stock solution. The catalyst ink was prepared by mixing the supported NP powder with the above stock solution such that the concentration was 1.0 mg mL^{-1} of powder in solution. The resultant mixture was then sonicated for 120 min. The catalyst ink (20 µL) was cast on a glassy carbon (GC) electrode (Pine Instruments, 5.0 mm diameter) using a micropipette and allowed to dry in air overnight while covered. Electrochemical studies were performed on a potentiostat (Autolab PGSTAT30) with a standard rotating electrode electrochemical cell. The rotating GC disk electrode with dried catalyst ink on its surface was used as the working electrode. Pt wire was used as the counter electrode and a saturated calomel electrode (SCE) was used as the reference electrode. All potentials were recorded with respect to the SCE. H$_2$SO$_4$ in ultra-pure water (0.5 M) was used as the electrolyte. To obtain the CO stripping curves, the catalyst was saturated with CO by bubbling CO in the electrolyte for 20 min with the electrode potential held at −0.2 V vs. SCE, followed by Ar-purging for 40 min. Two consecutive potential scans (20 mV s^{-1}) were then run to obtain the CO stripping and baseline curves. To obtain polarization curves for the electrooxidation of CO-contaminated H$_2$, the electrolyte was bubbled with a 1000 ppm CO–balance H$_2$ gas mixture for 60 min with the electrode potential held at −0.20 V vs. SCE, followed by a potential scan (1 mV s^{-1}) at a rotation rate of 1600 rpm.

Results

A series of rGO-supported Pt and PtSn nanoparticle catalysts were prepared from both commercial and synthetic rGOs to probe the metal-support influences on catalytic CO–H$_2$ electrooxidation. We compared Pt and PtSn catalysts because they are both well known hydrogen electrooxidation catalysts and their respective abilities to mitigate CO-poisoning effects are well

understood.[44–51] By using the same catalysts on different rGO supports, the relative shifts in H$_2$ oxidation onset with a well-defined CO impurity can be used as a measure of catalytic modification. To fully evaluate the series of rGOs, we used two commercial rGOs, known as functionalized graphene sheets (FGS) by Vorbeck Materials and single layer graphene (SLG) by ACS Material. In addition, we prepared two synthetic rGOs by reducing a synthetic graphene oxide (GO) with either borohydride or hydrazine. The hydrazine reduction method is known to induce pyrazole-type N-doping at the edges of the resulting graphene sheets whereas borohydride reductions give "pure" graphene without B or N doping.[8,14,15,20] These materials are denoted as NGO (N-doped reduced graphene oxide) and BGO (borohydride-reduced graphene oxide), respectively.

XPS (Fig. 1) and Raman microscopy studies (Fig. 2) show that the four rGOs have different degrees of reduction (i.e. graphene-like character) and a range of functional groups. From these data, the degree of graphitic-like character was evaluated using three different criteria: (1) the concentration of functional groups and defects from XPS data, (2) the FWHM value of the graphitic carbon C 1s peak, and (3) the degree of structural disorder through a comparison of the D and G peak intensities obtained from the Raman spectra. The normalized C 1s XPS spectra of the rGOs are shown in Fig. 1 and the data are summarized in Table 1. The comparative structural and spectroscopic data are summarized in Table 2.

The FGS, BGO, and NGO XPS C 1s spectra are very similar, featuring the expected intense peaks at 284.8 eV associated with graphitic type carbon (Fig. 1). While all of the rGOs have shoulders at higher binding energies due to various functional groups, the C–O peak for the SLG material is the most pronounced (Fig. 1b). Previous studies[8,11,13,14,52,53] have shown that hydrazine and borohydride reduction methods leave some unreacted carboxyl and hydroxyl groups, which is consistent with the small C–O, C(O)O and C=O peaks observed in our studies. The NGO spectrum also features a C–N peak consistent with the incorporation of nitrogen into the graphene structure.[13,15,54] The relative concentration of functional groups can be assessed by calculating the area ratio (C_g/C_f) of graphitic-type carbon, including $\pi \rightarrow \pi^*$ shake-up satellites (C_g) to total carbon associated with the functional groups (C_f). Excluding NGO, these data suggest that SLG is the most oxygenated, containing a large concentration of C–O moieties. FGS contains the fewest oxygen functionalities, with BGO intermediate between the two. After heat-treatment in H$_2$ atmosphere, there is a slight decrease in the C–O peaks for the SLG and BGO samples (Fig. S1†). Accordingly, the C_g/C_f value for each rGO sample increases (less functional groups) with the exception of FGS (Table S1†). Both observations are most likely due to a reduction of some hydroxyl groups during the H$_2$ atmosphere heat-treatment step.[7]

In addition to the oxygen-containing functional groups described above, NGO also contains 3.1% nitrogen resulting in 7.9% carbon-based C–N functional groups (Table 1). The N 1s spectrum of the NGO (Fig. S3†) shows three types of nitrogen-
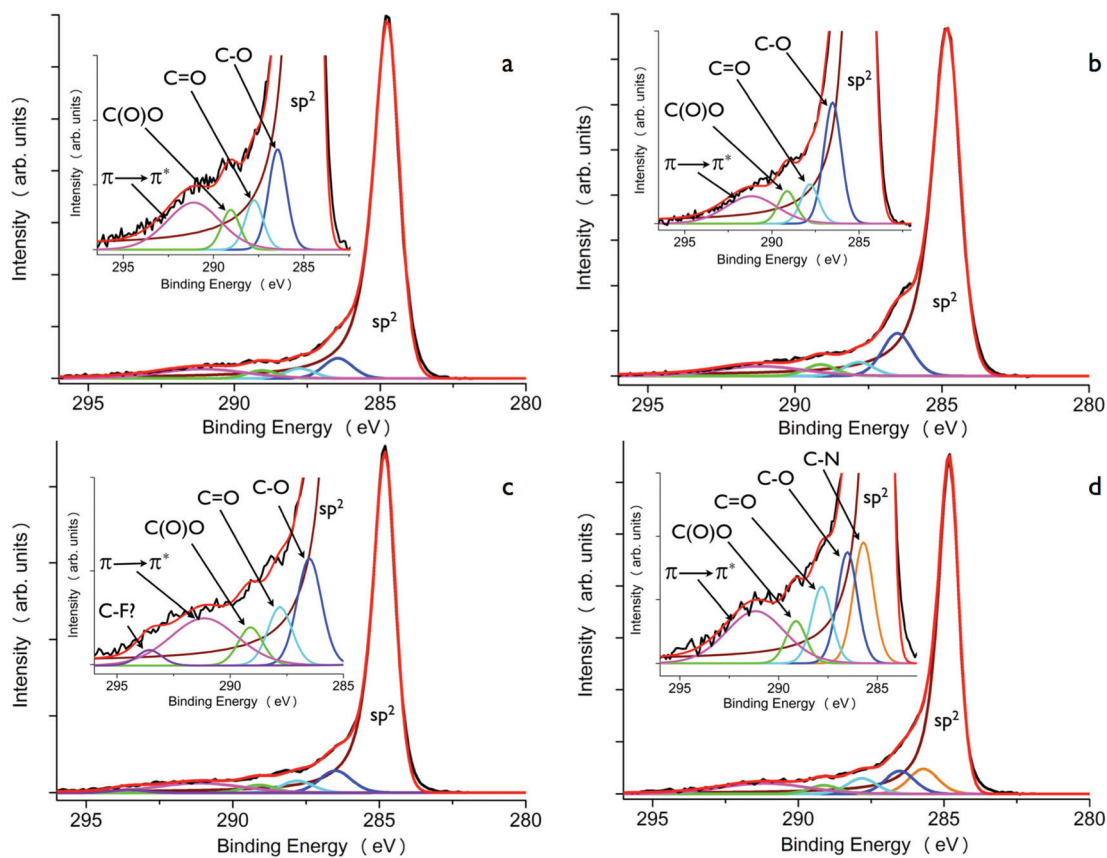
Fig. 1 Carbon 1s XPS spectra of the (a) FGS, (b) SLG, (c) BGO, and (d) NGO materials. The raw data (black) was fitted (red) according to the following functional groups: graphitic carbon (brown), C–N (orange), C–O (blue), C=O (cyan), C(O)O (light green), π→π* shake-up satellite (magenta). An unknown peak (purple) seen in the BGO sample is believed to arise from a small fluoride impurity (C–F, 1.08%).
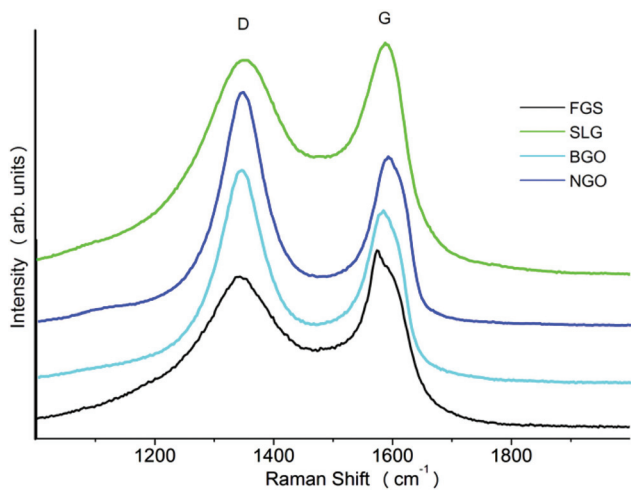

Fig. 2 Raman spectra of the different rGO materials.

Table 1 C 1s XPS peak position and relative peak area percentage of various functional groups in the rGOs

Sample	C–C/C=C	C–N	C–O	C=O	C(O)O	π→π*
FGS	284.8 eV (81.5%)	—	286.5 eV (5.6%)	287.8 eV (2.8%)	289.1 eV (2.2%)	291.1 eV (7.9%)
SLG	284.8 eV (75.5%)	—	286.5 eV (10.9%)	287.8 eV (3.5%)	289.1 eV (2.9%)	291.2 eV (7.2%)
BGO	284.8 eV (75.8%)	—	286.5 eV (7.4%)	287.8 eV (4.1%)	289.1 eV (2.7%)	291.2 eV (9.0%)
NGO	284.8 eV (67.1%)	285.7 eV (7.9%)	286.5 eV (7.3%)	287.8 eV (5.0%)	289.1 eV (2.8%)	291.2 eV (10.0%)

Table 2 Summary of evaluation criteria for the different rGOs

Sample	FWHM[a]	C_g/C_f[b]	D/G[c]
FGS	0.97	8.4	1.6
SLG	1.04	4.8	2.3
BGO	0.85	5.6	1.4
NGO	0.77	5.4	1.6

[a] C 1s XPS graphitic carbon peak FWHM (Fig. 1). [b] Graphitic carbon and π→π* shake-up satellites (C_g) and functionalized carbon (C_f) peak area percentages were used to determine C_g/C_f ratios (Table 1). [c] D/G ratios determined from integrating the D and G Raman peaks (Fig. 2).

containing species. The two major components at 399.3 eV and 400.8 eV are consistent with a pyrazole-like moiety whereas the minor peak at 402.7 eV is attributed to a quaternary-like nitrogen.[15,55] Similar results were obtained from analysis of the heat-treated NGO sample (Fig. S4†). These analyses (along with those below) suggest that the majority of nitrogen

is conjugated within the delocalized π-system of the graphene structure and remains in this state after high-temperature heat-treatment.

The conductivity of the rGOs can be correlated with the FWHMs of their respective graphitic carbon peak. Previous studies[56,57] have shown that a smaller FWHM value is associated with an increased degree of delocalization within the rGO. Our data (Table 2) suggest that the NGO is most conductive material (most graphene-like character), followed by the BGO, FGS, and SLG samples. This trend is essentially maintained after heat-treatment, except FGS appears to have slightly more graphene-like character than BGO after conditioning (Table S2†).

Raman spectroscopy provides a measure of structural disorder in graphene-based materials through a comparison of the graphite-like peak (G peak) to the disorder peak (D peak).[8,13,14,58] The disorder arises from intrinsic functional groups (ethers, epoxides, ketones), as well as atomic vacancies and defects, which affect the interactions with supported nanoparticle catalysts. Fig. 2 shows the Raman spectra of the rGOs, with the expected prominent D and G bands. The D/G ratios are listed in Table 2. Because the peak widths varied among the different rGOs, we calculated the D/G ratios by comparing the areas of the respective peaks and not the peak amplitudes. The rGOs examined here all have D/G ratios significantly greater than 1, which is similar to other graphene-like materials prepared from the reduction of GO.[14,29,54,59,60] These ratios suggest that BGO is the least defective material, followed by FGS and NGO with identical values whereas SLG has the highest defect concentration. After heat-treatment, all of the

rGO samples feature smaller D/G ratios, which are all very close to a value of 1 (Table S2†). This suggests the H_2 atmosphere heat-treatment induces some slight reduction of functional groups within the different rGO materials, in agreement with the XPS analysis as seen elsewhere.[61]

From these combined analyses (Table 2), we summarize the general characteristics of the rGOs as follows: (1) NGO is the most conductive rGO in our series and has few oxygen functional groups; the pyrazole-like nitrogen is presumably localized on the sheet edges[15] and does not appear to impart localizing defects into the structure; (2) FGS is equal to NGO in the level of disorder (D/G ratio) but FGS is less conductive and has the smallest number of oxygen-containing functional groups. The defects are presumably due to atomic vacancies associated with the FGS synthetic method;[5,6] (3) BGO has a greater amount of oxygen functionalities than FGS, but is more conductive. This ordering is reversed after heat-treatment; (4) SLG is the most defective rGO, with a high concentration of oxygen-containing functional groups and disorder and the lowest conductivity in the series. Overall, BGO is the most graphene-like in character (low FWHM, low D/G ratio, low functional group concentration), whereas NGO is the most conductive (lowest FWHM, low D/G ratio).

We prepared surfactant-free Pt and PtSn intermetallic ($P6_3/mmc$) NPs on the rGOs to evaluate the influence of the metal-support interactions. The rGO-supported PtSn intermetallic NPs were synthesized through modifications of our previous methods.[33,49] Specifically, $Pt(acac)_2$ and $SnCl_4$ were co-reduced in 1-octadecene using $NaBEt_3H$ in the presence of rGO at 200 °C. To transform the disordered PtSn alloy into its
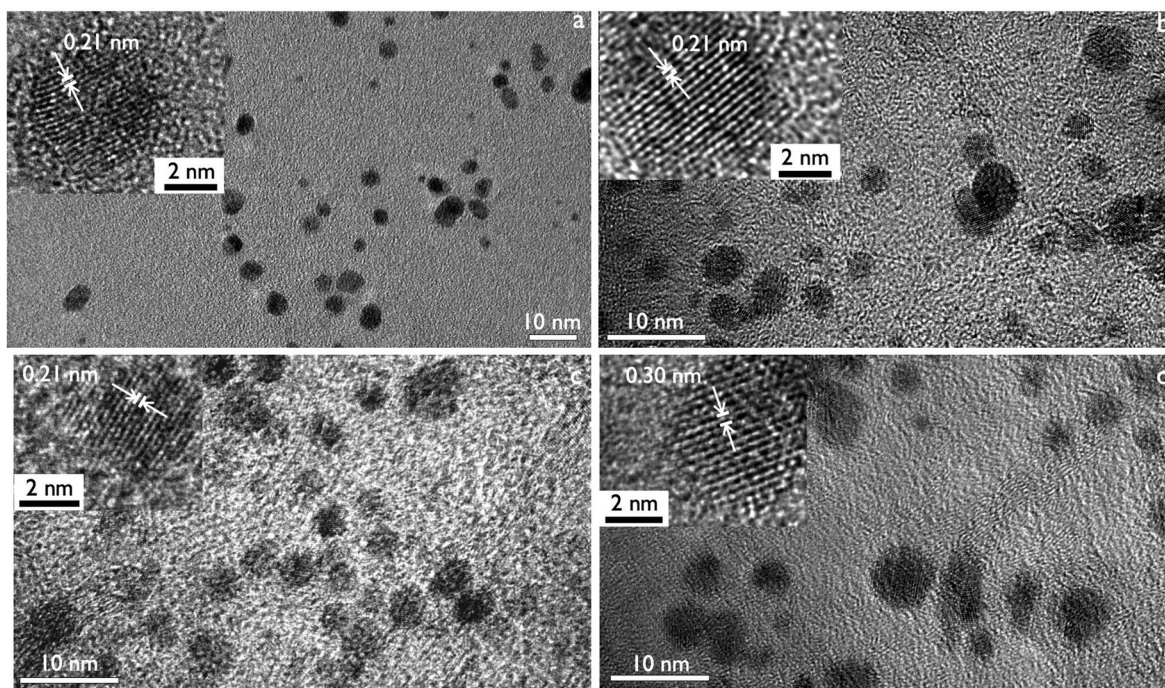

Fig. 3 TEM images of heat-treated PtSn intermetallic NPs supported on (a) FGS, (b) SLG, (c) BGO, and (d) NGO. Lattice fringe images of single particles are inset.
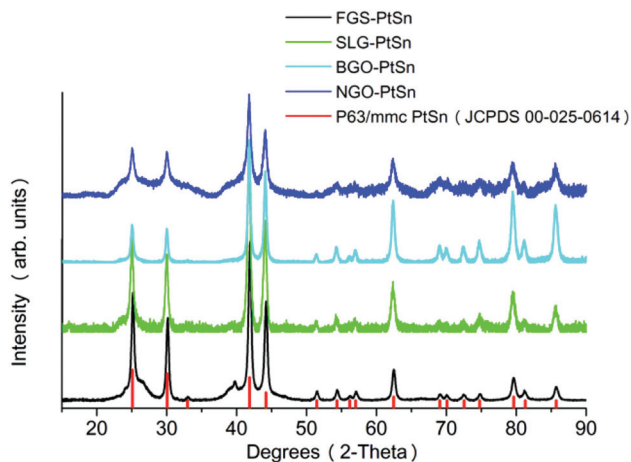
Fig. 4 XRD patterns of heat-treated rGO-PtSn intermetallic NPs. Red lines indicate the peak positions for hexagonal ($P6_3/mmc$) PtSn intermetallic (JCPDS 00-025-0614). The small peak at 40° in the FGS-PtSn sample is due to a small Pt_3Sn impurity. The broad low angle peaks (20−35°) are due to the rGOs.

ordered intermetallic phase, the supported particles were heat-treated for 2 hours at 400 °C under flowing H_2/Ar. While this procedure yielded the target PtSn intermetallic NPs, it also caused varying degrees of particle sintering. Many NPs remained in the sub-10 nm range (Fig. 3); however, agglomerates and aggregates of small particles make up a significant portion of the material (Fig. S5†). The synthetic procedure was optimized to keep particles as small as possible yet ensure complete transformation to the ordered PtSn intermetallic.

High-resolution images of the single particles reveal their intermetallic structure, with lattice fringe analysis showing average lattice separations of 0.21 nm and 0.30 nm, corresponding to the (102) and (101) planes, respectively, of the hexagonal ($P6_3/mmc$) PtSn intermetallic lattice (insets in Fig. 3). Fig. 4 shows the XRD patterns of the heat-treated particles, featuring intense diffraction peaks unique to the hexagonal ($P6_3/mmc$) PtSn intermetallic. EDS analysis of the PtSn intermetallic NPs shows they have an average 1 : 1 (Pt : Sn) composition, comparable to that of the initial precursor ratio (Fig. S6†).

The rGO-supported Pt electrocatalysts were synthesized using the same method as the PtSn NPs, except for the absence of the Sn precursor. These particles were also subjected to the same heat-treatment (400 °C for 2 hours under flowing H_2/Ar), with similar particle aggregations. For the SLG, BGO, and NGO supports, significant quantities of sub-10 nm particles are present (Fig. 5), but as with the PtSn NPs, significant particle aggregation occurs (Fig. S7b–d†). In contrast, particle sintering is minimal in the FGS-Pt sample, which features a relatively narrow size distribution centered on an average diameter of 2.8 nm (Fig. S7a†). Lattice fringe analysis from high-resolution images of the single particles shows average lattice separations of 0.22 nm, corresponding to the (111) planes of FCC Pt (insets in Fig. 5). The XRD patterns of the heat-treated particles are presented in Fig. 6, with diffraction peaks matching those of FCC Pt. The XRD pattern of the FGS-Pt sample features broader peaks relative to the other samples, in agreement with the TEM analysis suggesting minimal particle sintering from heat-treatment.

The electrocatalytic activities of the rGO-supported NPs were evaluated by CO-stripping cyclic voltammetry (CV) and
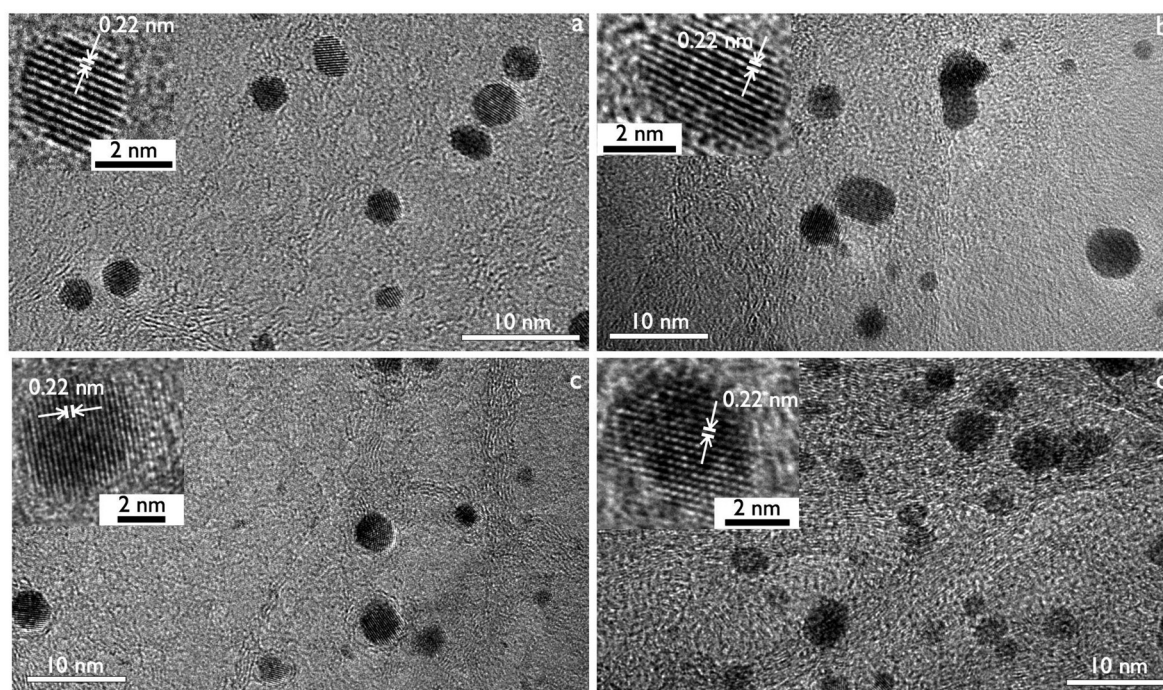

Fig. 5 TEM images of heat-treated Pt NPs supported on (a) FGS, (b) SLG, (c) BGO, and (d) NGO. Lattice fringe images of single particles are inset.
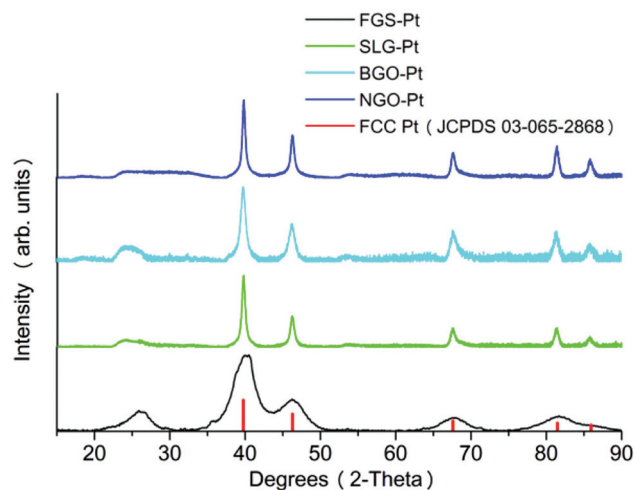
|

Fig. 6 XRD patterns of heat-treated rGO-Pt NPs. Red lines indicate the peak positions for FCC phase Pt (JCPDS 03-065-2868). Broad peaks (20–35°, 52–56°) are due to the rGOs.

Fig. 8 Polarization curves for the electrooxidation of CO-contaminated H_2 (1000 ppm CO, balance H_2) of rGO-Pt NP catalysts in 0.5 M H_2SO_4 solution. Red line indicates E-TEK Pt catalyst as reference. Curves were recorded at 25 °C with 1 mV s^{-1} scan rates and 1600 rpm rotation rates.

rotating disk electrochemical (RDE) experiments. The results are benchmarked against the commercial E-TEK Pt catalyst. All catalysts were prepared with a 30% total metal loading by weight. Prior to the electrochemical experiments, each catalyst was subjected to 10 potential scan cycles between −0.2 V and 0.8 V (*vs.* SCE) in 0.5 M H_2SO_4 saturated with Ar. Additional details are found in the experimental section. The CO stripping curves for each of the supported Pt catalysts show the characteristic CO oxidation peak near 0.5 V *vs.* SCE (Fig. 7).[62] However, the onset potentials for CO oxidation vary from 0.46 V (SLG-Pt) to 0.53 V for FGS-Pt and E-TEK Pt standard. The BGO-Pt and NGO-Pt catalysts are intermediate. Fig. 8 shows the RDE polarization curves for the electrooxidation of
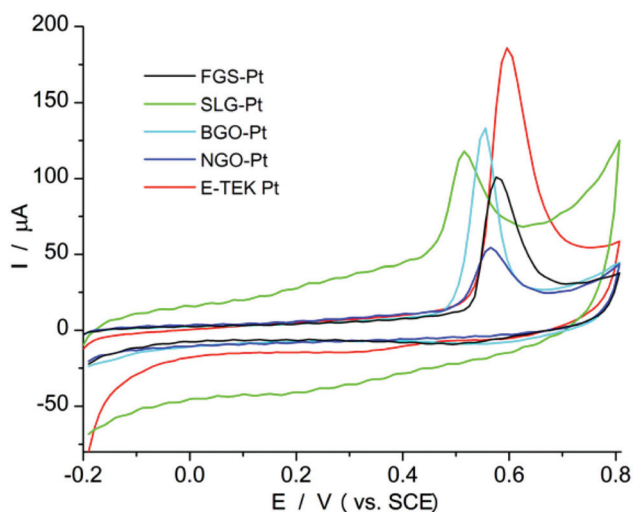
$CO–H_2$ mixtures (1000 ppm CO) on the Pt catalysts. The SLG-Pt and BGO-Pt show a 50 mV improvement in onset potentials relative to E-TEK Pt, whereas NGO-Pt and FGS-Pt are somewhat less CO tolerant than E-TEK Pt. In general, the rGO-Pt catalysts show the expected correlation between CO stripping onset and $CO–H_2$ electrooxidation onset where lower CO oxidation overpotentials give improved CO tolerance.

Since CO has a low affinity for binding to the PtSn surface, their CO-stripping curves are typically broad and of low intensity compared to their Pt counterparts (Fig. 9).[44,49,63,64] The solid lines represent the CO stripping curves while the dashed lines are the baselines recorded after the CO stripping experiments. For the FGS-PtSn sample (Fig. 9), two distinct peaks are observed at 0.35 V and 0.57 V, from CO oxidation and the oxidation of surface Sn, respectively.[49,50] Small Sn oxidation peaks are present in the BGO-PtSn and NGO-PtSn samples as well. Despite the ill-defined peak shapes, the onset potentials for CO oxidation can be discerned and varies from 0.08 V (NGO-PtSn) to 0.2 V (FGS-PtSn), with SLG-PtSn and BGO-PtSn intermediate.

Fig. 10 shows the polarization curves for the electrooxidation of $CO–H_2$ mixtures (1000 ppm CO) on the PtSn catalysts with the E-TEK Pt reference. The rGO-PtSn polarization onset potentials span 160 mV and are generally 200–400 mV lower than their rGO-Pt counterparts. The improvement in CO tolerance of the PtSn catalysts compared to the Pt systems is due to the "bifunctional mechanism" of CO oxidation and is consistent with previous studies.[49,62,65,66] The trends within the rGO-PtSn catalysts also follow those of the rGO-Pt samples (SLG > BGO > FGS) with the exception of the NGO-PtSn sample, where the CO tolerance is significantly increased compared to its Pt counterpart. The NGO-PtSn catalyst has the best performance of all the rGO-Pt or rGO-PtSn catalysts and surpasses the CO tolerance of the PtSn intermetallics supported

Fig. 7 CO stripping curves of rGO-Pt NP catalysts in 0.5 M H_2SO_4 solution at 25 °C. Red line indicates E-TEK Pt catalyst as reference. Scan rate: 20 mV s^{-1}.
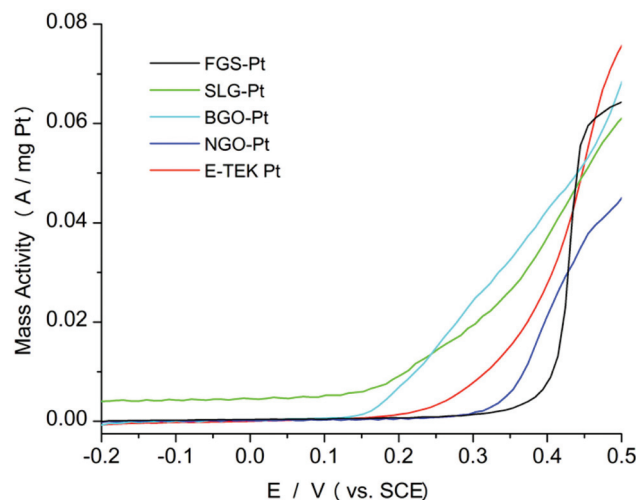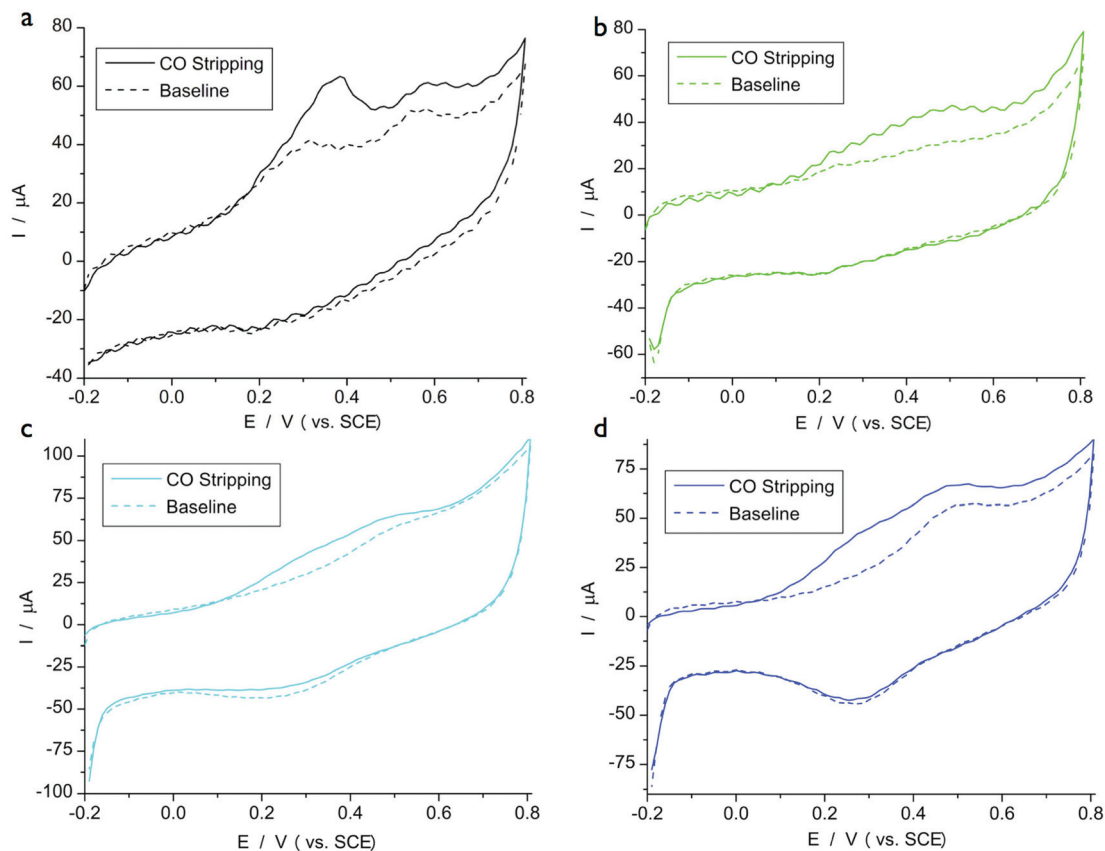
|

Fig. 9 CO stripping curves of (a) FGS, (b) SLG, (c) BGO, and (d) NGO supported PtSn intermetallic NP catalysts in 0.5 M H$_2$SO$_4$ solution at 25 °C. Scan rate: 20 mV s^{-1}. The dotted curves are the CVs recorded after CO stripping.
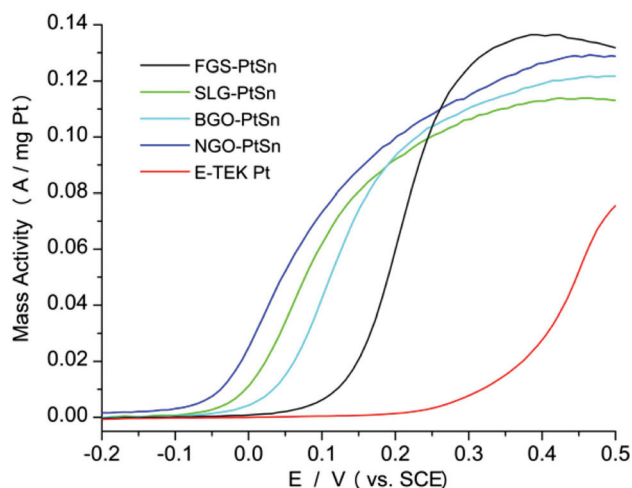

Fig. 10 Polarization curves for the electrooxidation of CO-contaminated H$_2$ (1000 ppm CO, balance H$_2$) of rGO-PtSn intermetallic NP catalysts in 0.5 M H$_2$SO$_4$ solution. Red line indicates E-TEK Pt catalyst as reference. Curves were recorded at 25 °C with 1 mV s^{-1} scan rates and 1600 rpm rotation rates.

Discussion

The synthetic, spectroscopic and electrochemical studies described above show that rGOs that are presumably quite similar in composition show a range of nanoparticle templating properties and can electronically influence electrocatalytic activity. These properties are summarized in Table 3. Two major tends emerge from the data.

First, the FGS support gives smaller Pt NPs with less agglomeration and sintering after annealing relative to the other rGO supports tested. This finding is consistent with the high level of defects found in FGS that presumably anchor the Pt seeds and NPs more tightly relative to the other rGO materials. Because we do not employ surfactants or dispersants, there is always some degree of agglomeration after sintering, but the FGS minimizes this sintering to a large degree. The templating effect of FGS extends to other monometallic NPs,[30,33] but is not apparent in the bimetallic PtSn system. The four rGO supports give similar PtSn particle sizes with no statistical differences in diameter or agglomeration.

Second, there is an apparent catalytic enhancement of the NGO-supported PtSn system relative to the other PtSn electrocatalysts. Previous studies have shown that PtSn electrocatalysts show a *ca.* 200 mV improvement in CO tolerance (ΔE_{onset}) relative to Pt catalysts of the same size on the same supports.[49]

on carbon black.[49] This improved CO tolerance is consistent with the CO stripping results, where NGO-PtSn also had the lowest onset potential for CO oxidation.

Table 3 Summary of representative experimental data for NP catalysts

Sample	Avg. NP size[a] (nm)	CO stripping E_{onset}[b]	CO stripping E_{peak}[b]	H$_2$–CO oxidation E_{onset}[b]	H$_2$–CO oxidation ΔE_{onset} ($E_{PtSn} - E_{Pt}$)
E-TEK Pt	N/A	0.53	0.59	0.20	—
FGS-Pt	2.8 ± 0.8	0.53	0.58	0.35	−0.27
FGS-PtSn	5.2 ± 3.9	0.20	c	0.08	
SLG-Pt	4.0 ± 2.0	0.46	0.52	0.15	−0.2
SLG-PtSn	4.4 ± 2.2	0.13	c	−0.05	
BGO-Pt	4.6 ± 2.6	0.49	0.56	0.15	−0.18
BGO-PtSn	4.2 ± 1.8	0.15	c	−0.03	
NGO-Pt	5.4 ± 3.0	0.52	0.57	0.33	−0.41
NGO-PtSn	5.6 ± 3.9	0.08	c	−0.08	

[a] Calculated by counting 100 small particles and agglomerates in Fig. S2 and S4. [b] Potential *vs.* SCE. [c] Not determinable from experimental data.

The SLG and BGO systems fall into this category (Table 3) showing 200 mV and 180 mV enhancements, respectively. The FGS catalysts show a somewhat larger ΔE_{onset} of 270 mV, but the larger shift most likely resides in the enhanced CO poisoning of the small Pt NPs[67] formed on the FGS support and large particle size differences between the Pt and PtSn particles. Somewhat surprisingly, there is a large 410 mV shift in ΔE_{onset} for the NGO Pt/PtSn system, despite the similarities in particle sizes of the Pt and PtSn NPs on this rGO support. In addition the NGO-supported PtSn NPs have sizes and agglomerates that are similar to the FGS-supported PtSn NPs, but have a 180 mV enhancement in CO tolerance. The possible origins of this enhancement are discussed below.

Previous theoretical studies have suggested that CO binds less tightly to Pt NPs supported on defective graphene (heteroatom inclusions, vacancies and disorder) relative to "pristine" graphene due to a downward shift in d-band center, resulting in increased CO tolerance.[38,68] Theoretical studies by Kim and Jhi suggest that doping of graphene with nitrogen weakens the Pt–CO bond on NGO-Pt NPs and improves their CO tolerance relative to un-doped graphene.[38] In contrast to these theoretical predictions, our work shows that the NGO-Pt catalyst has much lower CO tolerance compared to the nitrogen-free SLG and BGO analogues. However, the theoretical model employed by Kim and Jhi[38] analyzed the effects of pyridine-like nitrogen within the graphene structure, which does not appear to match the structure of the NGO used in our experiments. In a recent study, Park *et al.* showed that hydrazine reduction of GO results in the incorporation of pyrazole-like moieties into the graphene structure, which are primarily located on the edges of the graphene sheets.[15] Our analysis of NGO here is in agreement with their results. Other reports have suggested that the electronic effects of nitrogen incorporation may differ depending on the type of nitrogen substitution and the location of this substitution within the graphene structure.[15,38,69–73]

For PtSn intermetallic NPs, the nitrogen incorporation into the rGO support appears to lead to significant improvement in CO tolerance. It appears that the nitrogen or other defects in the NGO support have a substantially different interaction with the PtSn NPs relative to the pure Pt NPs. For example, it is possible that the surface Sn atoms form strong interactions with the NGO defect sites that drain electron density from the PtSn particle relative to the other rGOs. Such electron transfer would reduce Pt–CO bonding and increase CO tolerance. In our earlier work involving PtSn@Pt core–shell NPs, the PtSn intermetallic core modified the electronic structure of the Pt shell by shifting the d-band center, which promoted an improvement in CO tolerance.[49] The metal-support interactions in the present system may promote similar electronic modifications.

It is also possible that the anomalous activity enhancement for the NGO-PtSn system is a result of a spillover effect from the nitrogen, which can be viewed as an enhancement of the bifunctional mechanism of CO oxidation. The bifunctional mechanism proceeds *via* favorable OH binding to Sn surface atoms, which results in enhanced CO oxidation and improved CO tolerance.[48,66,74,75] A process that involves OH spillover from the NGO support onto the PtSn catalyst could enhance the bifunctional oxidation process. However, the lack of a similar enhancement in the corresponding NGO-Pt system suggests that OH spillover from the NGO support not likely. Rather, the enhancement is most likely a unique metal-support interaction between the PtSn intermetallic and the NGO support.

Our results here and in earlier experiments show that the CO tolerance enhancement for the PtSn intermetallic over pure Pt is consistently 180–270 mV lower when supported on nitrogen-free carbonaceous supports (CB, SLG, BGO, FGS).[49] Thus it appears that a unique 410 mV enhancement of the CO tolerance observed for NGO-PtSn relative to NGO-Pt results from a combination of electronic modifications due to PtSn intermetallic formation and the NGO-PtSn metal-support interaction. The origin of the enhancement may result from weakened Sn–OH bonding due to the increased electronic donation from the nitrogen dopants in NGO.[24,26,29,76] Such an increase could enhance CO tolerance by way of the bifunctional mechanism. In the pure Pt systems, however, increased donation from the NGO would only strengthen Pt–CO bonding and decrease CO tolerance. These opposing effects on the Pt *versus* PtSn systems are consistent with the anomalous ΔE_{onset} in the NGO system (Table 3).

Conclusions

In summary, we have developed a simple method for the production of both Pt and PtSn intermetallic NPs supported on various rGO materials without the use of additional surfactants or dispersants. Through RDE and CO stripping electrochemical experiments, we have shown that the rGO-PtSn catalyst is superior to the rGO-Pt catalyst regardless of the rGO material, in agreement with earlier reports on PtSn NP electrocatalysts. Our results also suggest that the catalytic activity is modulated by the rGO-catalyst support for the nitrogen-doped NGO. It appears that while BGO and SLG have different levels of functional group incorporation (C_g/C_f) and structural disorder (D/G), they show very similar metal-support interactions and catalytic performances for both the Pt and PtSn intermetallic systems. FGS appears to impart the strongest metal-support interactions, as evidenced by the lowest level of catalyst sintering of all rGOs tested. The NGO support is the most unusual since it seems to shift the CO tolerance in both directions depending on the electrocatalytic mechanism. For the NGO-PtSn system, CO tolerance may be enhanced through weakened Sn–OH bonding whereas CO tolerance from the NGO-Pt system is reduced due to stronger Pt–CO bonding. Further studies into the nature of these metal-support interactions are ongoing.

Acknowledgements

References

1 A. Peigney, C. Laurent, E. Flahaut, R. Bacsa and A. Rousset, *Carbon*, 2001, **39**, 507–514.

2 K. I. Bolotin, K. J. Sikes, J. Hone, H. L. Stormer and P. Kim, *Phys. Rev. Lett.*, 2008, **101**, 096802.

3 X. Fan, W. Peng, Y. Li, X. Li, S. Wang, G. Zhang and F. Zhang, *Adv. Mater.*, 2008, **20**, 4490–4493.

4 W. S. Hummers Jr. and R. E. Offeman, *J. Am. Chem. Soc.*, 1958, **80**, 1339–1339.

5 M. J. McAllister, J.-L. Li, D. H. Adamson, H. C. Schniepp, A. A. Abdala, J. Liu, M. Herrera-Alonso, D. L. Milius, R. Car, R. K. Prud'homme and I. A. Aksay, *Chem. Mater.*, 2007, **19**, 4396–4404.

6 H. C. Schniepp, J.-L. Li, M. J. McAllister, H. Sai, M. Herrera-Alonso, D. H. Adamson, R. K. Prud'homme, R. Car,

D. A. Saville and I. A. Aksay, *J. Phys. Chem. B*, 2006, **110**, 8535–8539.

7 A. Bagri, R. Grantab, N. V. Medhekar and V. B. Shenoy, *J. Phys. Chem. C*, 2010, **114**, 12053–12061.

8 W. Gao, L. B. Alemany, L. Ci and P. M. Ajayan, *Nat. Chem.*, 2009, **1**, 403–408.

9 S. Park, J. An, J. R. Potts, A. Velamakanni, S. Murali and R. S. Ruoff, *Carbon*, 2011, **49**, 3019–3023.

10 B. Seger and P. V. Kamat, *J. Phys. Chem. C*, 2009, **113**, 7990–7995.

11 X. Gao, J. Jang and S. Nagase, *J. Phys. Chem. C*, 2010, **114**, 832–842.

12 D. Long, W. Li, L. Ling, J. Miyawaki, I. Mochida and S.-H. Yoon, *Langmuir*, 2010, **26**, 16096–16102.

13 D. Yang, A. Velamakanni, G. Bozoklu, S. Park, M. Stoller, R. D. Piner, S. Stankovich, I. Jung, D. A. Field, C. A. Ventrice and R. S. Ruoff, *Carbon*, 2009, **47**, 145–152.

14 D. Luo, G. Zhang, J. Liu and X. Sun, *J. Phys. Chem. C*, 2011, **115**, 11327–11335.

15 S. Park, Y. Hu, J. O. Hwang, E.-S. Lee, L. B. Casabianca, W. Cai, J. R. Potts, H.-W. Ha, S. Chen, J. Oh, S. O. Kim, Y.-H. Kim, Y. Ishii and R. S. Ruoff, *Nat. Commun.*, 2012, **3**, 638.

16 M. A. Pope, C. Punckt and I. A. Aksay, *J. Phys. Chem. C*, 2011, **115**, 20326–20334.

17 C. Punckt, M. A. Pope, J. Liu, Y. Lin and I. A. Aksay, *Electroanalysis*, 2010, **22**, 2834–2841.

18 J. D. Roy-Mayhew, D. J. Bozym, C. Punckt and I. A. Aksay, *ACS Nano*, 2010, **4**, 6203–6211.

19 H. C. Schniepp, K. N. Kudin, J.-L. Li, R. K. Prud'homme, R. Car, D. A. Saville and I. A. Aksay, *ACS Nano*, 2008, **2**, 2577–2584.

20 H.-J. Shin, K. K. Kim, A. Benayad, S.-M. Yoon, H. K. Park, I.-S. Jung, M. H. Jin, H.-K. Jeong, J. M. Kim, J.-Y. Choi and Y. H. Lee, *Adv. Funct. Mater.*, 2009, **19**, 1987–1992.

21 S. O. Moussa, L. S. Panchakarla, M. Q. Ho and M. S. El-Shall, *ACS Catal.*, 2014, **4**, 535–545.

22 S. Bai, X. Shen, G. Zhu, M. Li, H. Xi and K. Chen, *ACS Appl. Mater. Interfaces*, 2012, **4**, 2378–2386.

23 S. Bong, Y.-R. Kim, I. Kim, S. Woo, S. Uhm, J. Lee and H. Kim, *Electrochem. Commun.*, 2010, **12**, 129–131.

24 L. Gao, W. Yue, S. Tao and L. Fan, *Langmuir*, 2013, **29**, 957–964.

25 S. Guo, D. Wen, Y. Zhai, S. Dong and E. Wang, *ACS Nano*, 2010, **4**, 3959–3968.

26 F. Han, X. Wang, J. Lian and Y. Wang, *Carbon*, 2012, **50**, 5498–5504.

27 W. He, H. Jiang, Y. Zhou, S. Yang, X. Xue, Z. Zou, X. Zhang, D. L. Akins and H. Yang, *Carbon*, 2012, **50**, 265–274.

28 D. He, K. Cheng, H. Li, T. Peng, F. Xu, S. Mu and M. Pan, *Langmuir*, 2012, **28**, 3979–3986.

29 Z. Ji, X. Shen, G. Zhu, K. Chen, G. Fu and L. Tong, *J. Electroanal. Chem.*, 2012, **682**, 95–100.

30 R. Kou, Y. Shao, D. Wang, M. H. Engelhard, J. H. Kwak, J. Wang, V. V. Viswanathan, C. Wang, Y. Lin, Y. Wang,

I. A. Aksay and J. Liu, *Electrochem. Commun.*, 2009, **11**, 954–957.

31 P. Kundu, C. Nethravathi, P. A. Deshpande, M. Rajamathi, G. Madras and N. Ravishankar, *Chem. Mater.*, 2011, **23**, 2772–2780.

32 C. Nethravathi, E. A. Anumol, M. Rajamathi and N. Ravishankar, *Nanoscale*, 2011, **3**, 569–571.

33 A. A. Ponce, C. M. Sims, Z. Liu, K. J. Gaskell, L. C. Lai, W. A. Chiou and B. W. Eichhorn, *J. Mater. Sci.*, 2012, **48**, 2670–2680.

34 C. V. Rao, A. L. M. Reddy, Y. Ishikawa and P. M. Ajayan, *Carbon*, 2011, **49**, 931–936.

35 C. Xu, X. Wang and J. Zhu, *J. Phys. Chem. C*, 2008, **112**, 19841–19845.

36 E. Yoo, T. Okada, T. Akita, M. Kohyama, I. Honma and J. Nakamura, *J. Power Sources*, 2011, **196**, 110–115.

37 X. Zhou, X. Huang, X. Qi, S. Wu, C. Xue, F. Y. C. Boey, Q. Yan, P. Chen and H. Zhang, *J. Phys. Chem. C*, 2009, **113**, 10842–10846.

38 G. Kim and S.-H. Jhi, *ACS Nano*, 2011, **5**, 130710093934005–130710093934810.

39 Y. Okamoto, *Chem. Phys. Lett.*, 2006, **420**, 382–386.

40 E. Yoo, T. Okata, T. Akita, M. Kohyama, J. Nakamura and I. Honma, *Nano Lett.*, 2009, **9**, 2255–2259.

41 R. W. Joyner, J. B. Pendry, D. K. Saldin and S. R. Tennison, *Surf. Sci.*, 1984, **138**, 84–94.

42 S. J. Tauster, *Acc. Chem. Res.*, 1987, **20**, 389–394.

43 *Catalysis and Electrocatalysis at Nanoparticle Surfaces*, ed. A. Wieckowski and E. R. Savinova, CRC Press, 1st edn, 2003.

44 M. Arenz, V. Stamenkovic, B. B. Blizanac, K. J. Mayrhofer, N. M. Marković and P. N. Ross, *J. Catal.*, 2005, **232**, 402–410.

45 A. C. Boucher, N. Alonso-Vante, F. Dassenoy and W. Vogel, *Langmuir*, 2003, **19**, 10885–10891.

46 G. A. Camara, E. A. Ticianelli, S. Mukerjee, S. J. Lee and J. McBreen, *J. Electrochem. Soc.*, 2002, **149**, A748–A753.

47 H. Igarashi, T. Fujino, Y. Zhu, H. Uchida and M. Watanabe, *Phys. Chem. Chem. Phys.*, 2001, **3**, 306–314.

48 S. Lee, S. Mukerjee, E. Ticianelli and J. McBreen, *Electrochim. Acta*, 1999, **44**, 3283–3293.

49 Z. Liu, G. S. Jackson and B. W. Eichhorn, *Angew. Chem., Int. Ed.*, 2010, **49**, 3173–3176.

50 Z. Liu, D. Reed, G. Kwon, M. Shamsuzzoha and D. E. Nikles, *J. Phys. Chem. C*, 2007, **111**, 14223–14229.

51 T. Schmidt, H. Gasteiger, G. Stab, P. Urban, D. Kolb and R. Behm, *J. Electrochem. Soc.*, 1998, **145**, 2354–2358.

52 P.-G. Ren, D.-X. Yan, X. Ji, T. Chen and Z.-M. Li, *Nanotechnology*, 2011, **22**, 055705.

53 V. Singh, D. Joung, L. Zhai, S. Das, S. I. Khondaker and S. Seal, *Prog. Mater. Sci.*, 2011, **56**, 1178–1271.

54 I. K. Moon, J. Lee, R. S. Ruoff and H. Lee, *Nat. Commun.*, 2010, **1**, 1–6.

55 A. Katrib, N. R. El-Rayyes and F. M. Al-Kharafi, *J. Electron Spectrosc. Relat. Phenom.*, 1983, **31**, 317–321.

56 R. Rozada, J. I. Paredes, S. Villar-Rodil, A. Martínez-Alonso and J. M. D. Tascón, *Nano Res.*, 2013, **6**, 216–233.

57 S. Villar-Rodil, J. I. Paredes, A. Martínez-Alonso and J. M. Tascón, *J. Mater. Chem.*, 2009, **19**, 3591–3593.

58 A. C. Ferrari, *Solid State Commun.*, 2007, **143**, 47–57.

59 D. Geng, Y. Chen, Y. Chen, Y. Li, R. Li, X. Sun, S. Ye and S. Knights, *Energy Environ. Sci.*, 2011, **4**, 760–764.

60 Y. T. Liang, B. K. Vijayan, K. A. Gray and M. C. Hersam, *Nano Lett.*, 2011, **11**, 2865–2870.

61 A. Bagri, C. Mattevi, M. Acik, Y. J. Chabal, M. Chhowalla and V. B. Shenoy, *Nat. Chem.*, 2010, **2**, 581–587.

62 H. Gasteiger, N. Markovic, P. Ross and E. J. Cairns, *J. Phys. Chem.*, 1994, **98**, 617–625.

63 E. M. Crabb, R. Marshall and D. Thompsett, *J. Electrochem. Soc.*, 2000, **147**, 4440–4447.

64 D. Lee, S. Hwang and I. Lee, *J. Power Sources*, 2005, **145**, 147–153.

65 B. E. Hayden, M. E. Rendall and O. South, *J. Am. Chem. Soc.*, 2003, **125**, 7738–7742.

66 K. Wang, H. Gasteiger, N. Markovic and P. Ross, *Electrochim. Acta*, 1996, **41**, 2587–2593.

67 S. Guerin, B. E. Hayden, C. E. Lee, C. Mormiche, J. R. Owen, A. E. Russell, B. Theobald and D. Thompsett, *J. Comb. Chem.*, 2004, **6**, 149–158.

68 I. Fampiou and A. Ramasubramaniam, *J. Phys. Chem. C*, 2012, **116**, 6543–6555.

69 Z. Luo, S. Lim, Z. Tian, J. Shang, L. Lai, B. MacDonald, C. Fu, Z. Shen, T. Yu and J. Lin, *J. Mater. Chem.*, 2011, **21**, 8038–8044.

70 N. Mahmood, C. Zhang, F. Liu, J. Zhu and Y. Hou, *ACS Nano*, 2013, **7**, 10307–10318.

71 J. P. Paraknowitsch and A. Thomas, *Energy Environ. Sci.*, 2013, **6**, 2839–2855.

72 S. Pylypenko, A. Borisevich, K. L. More, A. R. Corpuz, T. Holme, A. A. Dameron, T. S. Olson, H. N. Dinh, T. Gennett and R. O'Hayre, *Energy Environ. Sci.*, 2013, **6**, 2957–2964.

73 A. L. M. Reddy, A. Srivastava, S. R. Gowda, H. Gullapalli, M. Dubey and P. M. Ajayan, *ACS Nano*, 2010, **4**, 6337–6342.

74 H. A. Gasteiger, N. M. Marković and P. N. Ross Jr., *J. Phys. Chem.*, 1995, **99**, 8945–8949.

75 H. A. Gasteiger, N. M. Marković and P. N. Ross, *Catal. Lett.*, 1996, **36**, 1–8.

76 W.-P. Zhou, W. An, D. Su, R. Palomino, P. Liu, M. G. White and R. R. Adzic, *J. Phys. Chem. Lett.*, 2012, **3**, 3286–3290.